Naval Research Laboratory
Stennis Space Center, MS 39529-5004

Airborne Scanning Lidar Measurement of Ocean Waves

PAUL A. HWANG

Ocean Sciences Branch
Oceanography Division

WILLIAM B. KRABILL
WAYNE WRIGHT
NASA/GFSC Laboratory for Hydrospheric Processes
Wallops Island, VA

EDWARD J. WALSH
NASA/GFSC Laboratory for Hydrospheric Processes
Wallops Island, VA
Presently Assigned at NOAA Environmental Technology Laboratory
Boulder, CO

ROBERT N. SWIFT
EG&G Services, Inc.
Wallops Island, VA

March 9, 1999

1999 0326 039

DTIC QUALITY INSPECTED 4

REPORT DOCUMENTATION PAGE

Form Approved
OBM No. 0704-0188

1. AGENCY USE ONLY *(Leave blank)*	2. REPORT DATE March 9, 1999	3. REPORT TYPE AND DATES COVERED Final

4. TITLE AND SUBTITLE

Airborne Scanning Lidar Measurement of Ocean Waves

6. AUTHOR(S)

Paul A. Hwang, *William B. Krabill, *Wayne Wright, **Edward J. Walsh, and †Robert N. Swift

5. FUNDING NUMBERS

Job Order No. 73-T019-99

Program Element No. 0602435N

Project No.

Task No. BE-35-2-46

Accession No.

7. PERFORMING ORGANIZATION NAME(S) AND ADDRESS(ES)

Naval Research Laboratory
Oceanography Division
Stennis Space Center, MS 39529-5004

8. PERFORMING ORGANIZATION REPORT NUMBER

NRL/MR/7332--99-8221

9. SPONSORING/MONITORING AGENCY NAME(S) AND ADDRESS(ES)

Office of Naval Research
800 N. Quincy St.
Arlington, VA 22217-5000

10. SPONSORING/MONITORING AGENCY REPORT NUMBER

11. SUPPLEMENTARY NOTES
*NASA/GFSC Laboratory for Hydrospheric Processes, Wallops Island, VA 23337
**NASA/GFSC Laboratory for Hydrospheric Processes, Wallops Island, VA, presently on assignment at NOAA Environmental Technology Laboratory, Boulder, CO 80303
†EG&G Services, Inc., N159, Wallops Flight Facility, Wallops Island, VA 23337

12a. DISTRIBUTION/AVAILABILITY STATEMENT

Approved for public release; distribution unlimited.

12b. DISTRIBUTION CODE

13. ABSTRACT *(Maximum 200 words)*

A scanning lidar system provides high-resolution, two-dimensional measurements of ocean wave displacement. The fact that it is an airborne operation further enhances the speed of data acquisition. These properties allow rapid characterization of the ocean wave environment. In addition to active ranging, the scanning optics can obtain passive measurements of surface emissivity, yielding a digital image of surface brightness in real time. Processed into a binary image, these measurements can provide information on the average statistics and the spatial distribution of breaking waves. Technical specifications of the system and examples of application are presented.

14. SUBJECT TERMS

nonlinear, phase resolved, waves, littoral

15. NUMBER OF PAGES
21

16. PRICE CODE

17. SECURITY CLASSIFICATION OF REPORT	18. SECURITY CLASSIFICATION OF THIS PAGE	19. SECURITY CLASSIFICATION OF ABSTRACT	20. LIMITATION OF ABSTRACT
Unclassified	Unclassified	Unclassified	SAR

Airborne Scanning Lidar Measurement of Ocean Waves

ABSTRACT

A scanning lidar system provides high-resolution two-dimensional measurements of ocean wave displacement. The fact that it is an airborne operation further enhances the speed of data acquisition. These properties allow rapid characterization of the ocean wave environment. In addition to active ranging, the scanning optics can obtain passive measurements of surface emissivity, yielding a digital image of surface brightness in real time. Processed into a binary image, these measurements can provide information on the average statistics and the spatial distribution of breaking waves. Technical specifications of the system and examples of application are presented.

1. INTRODUCTION

Laser ranging was introduced for airborne ocean wave measurement in the '70s (Schule et al. 1971; Hoge et al. 1980). Using the high-resolution, profiling (one-dimensional) mode, Schule et al. (1971) obtained transect wavenumber spectrum in the wind direction to study the wave growth mechanism and the properties of wavenumber spectrum (see also discussions in Phillips 1977, Ch. 4). Since then, many improvements have been incorporated into the design of newer generations of airborne lidars. The most significant advances include the two-dimensional scanning capability (Krabill et al. 1995 a, b) and the correction for aircraft motion using the kinematic global positioning system (GPS) technique (Krabill and Martin 1987). Although these improvements were supported mainly by the Greenland ice research, the technology is obviously also suitable for measuring the topography of ocean surface waves.

Most recently, a new capability was added to the system that uses the laser scanning optics in passive mode to collect a digital image of the ground or ocean surface. This latest addition is useful for analyzing the spatial distribution of breaking patches on the ocean surface. In addition to the lidar system, video images or 70 mm photographs are routinely collected during each airborne measurement mission. The combination of active ranging, passive imaging, and continuous video recording of the ocean surface is a powerful tool for the study of ocean wave dynamics on the continental shelf. In section 2, we provide a brief description of the measurement system. Section 3 describes three data sets collected in two field experiments (Duck94 and SandyDuck97) organized by the Office of Naval Research and the U. S. Army Corps of Engineers (Birkemeier et al. 1994, 1996). Section 4 presents a few possible applications of airborne scanning lidar data in ocean wave research. Section 5 summarizes the paper with concluding remarks.

2. MEASUREMENT SYSTEM

The key instrument of the ocean wave measurement system described in this paper is the airborne topographic mapper (ATM). This is an airborne scanning lidar ranging system originally designed for monitoring annual variations in the Greenland ice sheet. The hardware design has been described elsewhere (Krabill et al. 1995 a, b). Here we only discuss briefly the scanning method and the technical specifications of the vertical and horizontal resolutions.

The ATM measures the range between the aircraft and the surface of the ground or ocean. It uses a nutating scanning mirror to project the laser beam in a circular pattern on the surface with a 15° incident angle. Carried on a moving aircraft, the locus of the scanning pattern is an approximately oval shape with the major axis in the cross-track direction and the minor axis in the along-track direction. The repetition rate of the azimuthal scanning cycles is 10 Hz. The laser is pulsed at 5 kHz so there are 500 range measurements evenly spaced around each scan cycle. These are interlaced with 500 passive digital measurements of the surface emissivity. The operational altitude of the aircraft is typically between 400 and 600 m. With a 1 mrad dispersion angle for the laser beam, the footprint of the laser spot on the ocean surface is between 0.4 and 0.6 m. The swath of the image is between 200 and 300 m, and the spacing

between neighboring active and passive image pixels is between 1.3 and 1.9 m. The vertical resolution of the ranging is dictated by the determination of the aircraft's position. The theoretical accuracy of the kinematic GPS system is 0.01 to 0.02 m. Dynamic calibration of the GPS measurements and the laser ranging to a calm water body shows that the rms error of the vertical resolution is actually better than 0.08 m. The total error budget for an individual laser footprint location currently is comprised of ~3 cm (rms) for range, 5cm for GPS position, and 5cm for attitude induced errors (Krabill and Martin 1987).

Figure 1 shows a comparison of the surface wave topography derived by a scanning lidar and a 70 mm photograph of the ocean surface taken nearly simultaneously. The high-fidelity measurement of the ocean waves is quite evident. In this figure, the horizontal coverage of the photograph (67° viewing angle) is more than twice the width of the laser swath. The corresponding region of the laser image is outlined by a rectangular box in the photograph for easy comparison. The nonlinear features, such as the narrow crests and flattened troughs of these shoaling waves in the coastal region, can be clearly identified in both sets of images. Other detailed features, such as the distortion of the wave fronts and the "forks" at approximately one-third from the bottom of the images, are faithfully depicted in the lidar topography. Even the scalloped shape of the coastline is faithfully captured.

For quantitative analyses of the wave data, the circular scanning data are resampled into rectangular grids. Because the data are sparser near the central region than that near two edges, the rectangular grid size is dictated by the spacing in the central region. This spacing is determined by the speed of the aircraft and the laser scan rate. The repetition rate of the scanning cycles is 10 Hz, therefore the scanning arc advances every 0.1 s in the along-track direction. The typical speed used in the wave mapping missions was either 60 or 100 m s^{-1} depending on the aircraft used, which translates to a grid size of 6 to 10 m along the track. The cross-track grid size can be maintained at the original scanning spacing (1.3 to 1.9 m). A more detailed analysis of the mapping of circular scanning data into rectangular grids is presented in the Appendix A.

3. DESCRIPTION OF FIELD EXPERIMENTS

The ATM system participated in Duck94 and SandyDuck97 and completed three flight missions. Figure 2 is a map of the experimental area and the local bathymetry. The width of the continental slope in the region is approximately 100 km. The bathymetric changes are relatively mild. The flight pattern in Duck94 included both along-shore and cross-shore tracks. Some of the tracks extended to more than 80 km offshore. During SandyDuck97, the aircraft flew a repeated racetrack pattern with two long tracks approximately perpendicular to the bathymetry contours. The seaward extent of the tracks is 40 km from the coastline. The cross-shore tracks of SandyDuck97 are shown in Figure 2.

During Duck94, a NASA P3 aircraft was used. The flight speed varied from 90 to 105 m s^{-1}. The measurements were acquired on 17 and 18, October 1994, with a flight time of 2 and 3 hours, respectively. Prior to the flight, on 15 October, a major extratropical storm arrived in the area with wind speeds reaching 20 m s^{-1} from the north. The wind speed and wind direction recorded by the anemometer installed at the end of the pier (approximately 600 m offshore) of the U. S. Army Field Research Facility are shown in Figures 3a and b. During the flight period on 17 October, the wind had decreased to approximately 9 m s^{-1} from the north. The significant wave height measured by a wave buoy located 4 km offshore was approximately 2.1 m and the peak wave period was between 10 and 11 s (Figures 3c and d). On October 18, the wind further decreased to 0 to 3 m/s during the flight period. The wave height was approximately 1.9 m and the peak wave period was between 10.5 and 11.5 s (Figures 3c and d). In both missions, the wave systems were dominated by the swell generated by the earlier storm. The aircraft performed similar flight patterns for both days, with 4 to 5 tracks along the coastline mapping the surf zone (the images shown in Figure 1 were from one of the surf zone mapping tracks), two tracks almost perpendicular to the coastline, and two tracks oblique to the coastline. The lengths in the cross-shore segments of the tracks varied from 20 to 80 km.

During SandyDuck97, the aircraft (a NOAA Twin Otter) flew for 4 hours (from 0700 to 1100 EST) on 24 September 1997. A front had passed through the area the night before. Wind speed increased from

4 to 12 m s^{-1} within a two hour period (2230 EST September 23 to 0030 EST September 24) and wind direction shifted from westerly to northerly (Figures 4a and b). The wind speed was quasisteady at approximately 9.5 m s^{-1} from 0200 to 0900 EST 24 September, and then gradually decreased from 9.5 to 7.5 m s^{-1} during the second half of the mission. This front generated a new wave system with the significant wave height increasing rapidly from 0.5 to 1.2 m within 2 hours in response to the rapid increase in wind speed (Figure 4c). The peak wave period also increased from 2.5 to 5 s during the frontal passage (Figure 4d). For the first two hours of the flight (0700 to 0900), waves continued to grow at a lesser pace. For the last two hours, the wave field decayed following the decrease in wind speed. The aircraft flew a race track pattern with the two long legs approximately perpendicular to the coastline (Figure 2). Altogether, the aircraft accomplished six repeat mappings on one leg and seven on the other leg. The time interval between repeating visits on each leg was approximately 0.5 hour, and the aircraft speed was approximately 60 m s^{-1}. The altitude of the flight alternated between 450 m and 600 m.

The passive digital surface imaging capability was not available during the Duck94 experiment. Instead, contiguous 70 mm photographs were taken during the along-beach flight lines. In addition, a scanning radar altimeter (SRA) was carried on the NASA P3. For SandyDuck97, video recording replaced 70 mm photographs and passive digital images from the scanner were also available. In the following section we present examples of the data to illustrate a few applications of these spatial and temporal measurements of the surface wave field.

4. APPLICATIONS FOR WAVE RESEARCH

The data sets described in the last section cover a small yet interesting cross section of the environmental conditions. The first data set (17 October 1994) represents a wind generated sea on background swell. The second data set (18 October 1994) is an ideal swell condition. The third data set (24 September 1997) covers the conditions of steady and active wind generation (0700 to 0900) and decaying wind waves (0900 to 1100). These data sets will be referred to hereafter as data sets I, II, IIIa, and IIIb, respectively. Because these are continuous spatial measurements over tens of kilometers across the continental shelf or in the surf zone, they offer a unique opportunity for the study of wave dynamics and wave kinematics in a littoral region with bathymetric features.

4.1. Wavenumber spectrum

The most obvious utilization of these two-dimensional measurements of ocean surface topography is the direct computation of the vector wavenumber spectrum. Figure 5a shows a 20-s segment of the surface topography covering an area approximately 180 m × 1400 m. The data were collected on 24 September 1997 starting at 09:35:11. The resampled rectangular grid size is 6 m in the along-track (x) direction and 3 m in the cross-track (y) direction. The wave pattern can be easily identified. The two-dimensional wavenumber spectrum can be calculated using a standard 2-D FFT procedure. (The results presented in this paper are processed using MATLAB.) Figure 5b shows an example of the wavenumber spectrum computed from an image segment of 180 m × 200 m. Even with an image of this small size, the dominate wavelength and propagation direction are clearly identified in both the spatial plot and the wavenumber spectrum. This is an equivalent of 3 s flight data and illustrates the capability of rapid characterization of surface wave properties using an airborne scanning lidar.

One can apply ensemble or bin averaging to increase the statistical confidence of the spectral estimate. Figure 5c is a smoothed spectrum of the one displayed in Figure 5b. The smoothing is over a 3×3 grid mask with a weighting function of 1/4 for the central cell, 1/8 for the four neighboring cells, and 1/16 for the four corner cells. The degrees of freedom of the new spectrum are 18 as compared to 2 for the raw spectrum. The result of ensemble averaging of seven consecutive image segments is shown in Figure 5d. The spectrum obtained by both ensemble averaging (of seven) and bin averaging (of nine) is shown in Figure 5e, which results in a reasonably smooth spectrum. In either case, the spectral properties of the dominant waves are easily determined from the two-dimensional spatial measurement of surface

elevation.

The spectra plotted in Figures 5b-e represent the encounter spectra as observed from the moving aircraft. Due to the relative velocity of the aircraft and the wave propagation, the wavelength will appear longer when the aircraft moves in the direction of wave propagation, and shorter when it travels in the opposite direction. The fractional error in wavelength estimate is the ratio between the wave phase speed and the aircraft velocity. In addition to the relative motion of the aircraft and the wave field, any difference between the aircraft heading and the ground track orientation requires a drift angle correction in the resulting wavenumber spectrum. Walsh et al. (1985) present a detailed analysis and correction procedures for the relative motion and the aircraft heading. Because these corrections are phase-velocity dependent, the resulting wavenumber grids are no longer in equal spacing, thus making graphic presentation rather difficult. We will not attempt to plot the two-dimensional spectrum in the corrected wavenumber space. In the present case, the phase speed of 6-s waves is 9 m s^{-1} and the speed of the aircraft is 60 m s^{-1}. The wavelength correction at the spectral peak is approximately 15 %. Figure 6 shows the comparison of the omni-spectra (integrated over all angles in the half plane of the corrected two-dimensional spectrum) with and without Doppler shift and drift angle correction. The significant wave height calculated from the ATM data is 1.44 m. The corrected peak wavenumber of this wave field (Figure 5a) is 0.10 rad m^{-1} (the peak wavelength L_p=61 m). The propagation direction is approximately 40° with respect to the flight track, which is almost perpendicular to the coastline (Figure 2). These are consistent with buoy measurements (at 900 m offshore) of the significant wave height (1.30 m), peak wave period (6.5±0.5 s, corresponding to L_p=66±10 m), and the northeasterly wind direction that generated this wave system.

4.2. Wave transformation in the coastal region

Continuous mapping of surface waves provides comprehensive coverage of the shoaling process. This is especially valuable for studying wave transformation in regions with bathymetric features. Figure 7 shows two images of the surface wave field in a region extending to approximately 1.3 km from the coastline (offshore is to the right of the images). The swath of the coverage is approximately 300 m. The two images are obtained by separating the front and rear halves of the circular scan cycles. This area is the nearshore section of a long track that extends to more than 70 km offshore (data set I). The evolution of the wave field during the shoaling process is recorded continuously in space. The variation in wavelength, wave height, and propagation direction can be analyzed from segments of these images.

The nature of continuous spatial mapping offers a convenient way to investigate the sink and source functions governing wave dynamics. For example, Hwang et al. (1998) analyze a 76-km track (perpendicular to the coastline) of the SRA data collected on 18 October 1994 to study the dissipation of shoaling swell. Since the wave condition is an ideal swell propagation (wave period 12 s, wave height 2 m measured by a buoy 4 km offshore) and wind speed is low (0-3 m s^{-1}), the swell can be treated as a one-dimensional progressive wave system with bottom friction as the only sink term. The energy balance equation is

$$\frac{\partial (EC_g)}{\partial x} = -\varepsilon = -\beta E$$

(1)

where E is wave energy, C_g is wave group velocity, x is in the wave propagation direction, which coincides with the flight track orientation, ε is energy dissipation rate, and β is energy dissipation coefficient. Spectral analysis is applied to determine the cross-shore distribution of swell energy and the dominant wavelength. The latter is used to calculate the group velocity, given the water depth profile and the known swell frequency. From continuous spatial measurements, the energy flux, flux gradient, and dissipation rate are readily obtained based on (1). The results indicate that the lower bounding of the dissipation coefficients calculated from the SRA data is in excellent agreement with the prediction of bottom friction based on a quadratic shear stress formulation (Thornton and Guza 1983; Hwang et al.

1998, Figure 8). These results were obtained using the SRA data with a horizontal resolution of 10 m and vertical resolution of 0.2 m. The resolution of ATM is considerably better than that of the SRA. The processing of ATM data is now in progress and will be used to refine the dissipation calculation of the swell case as well as other wave conditions now available.

4.3. Time/space lag measurements and correlation function

As noted earlier, the front and rear halves of the circular scanning cycles produce separate ocean surface images (Figures 7a, b). The two images represent two time-lapsed pictures of the surface waves. In other words, a given position visited by a certain laser beam in the front half of the scanning cycle will be revisited by a conjugate laser beam in the rear half of the scanning cycle. The time lag, however, is not a constant across the flight track. It can be calculated from the separation distance between the pairs of laser spots that hit the same position on the surface divided by the aircraft speed. For a typical flight configuration, this time lag varies from approximately 2 s at the center of the flight track to one digitization time step (1/5000 s) at the two edges. A different way of viewing the variable time lags is to treat the 500 points on a scan cycle as 250 pairs of sensing probes formed by the fore and aft halves of the scan pattern. The spatial lag in the along-track direction between each pair varies from 1.3 m at the edges to 200 m at the center of the scan cycle for an aircraft operating at a 400 m altitude and 60 m s^{-1} airspeed. A more detailed analysis of the temporal and spatial lags is given in Appendix A.

The capability of obtaining such a large number of paired measurements in the ocean is indeed exciting. Data sequences from these pairs can be sorted according to the spatial lag. Several possibilities for using such data include investigation of the spatial or temporal correlation of a wave field. The information can be used to study the evolution of wave pattern over small time/space steps. The time/space lapse images also offer an additional piece of information on the direction of wave propagation to eliminate the 180° directional ambiguity (of the axisymmetric spectral lobes) that typically occurs in the processing of two-dimensional images. Although the Doppler effect of airborne measurements allows such discrimination by using two tracks that differ by 90° or more (Walsh et al. 1985), with the time/space lapse images the discrimination can be achieved using measurements from a single track. There are several approaches to exploiting the time/space lag information to eliminate the 180° ambiguity in the 2D wavenumber spectrum. One of the easiest ways is to calculate the correlation coefficient or the coherence function of the two space series. An example of the computed cross correlation coefficients from a pair of data sequences in the midsection of the swath is shown in Figure 8. The autocorrelation of the front "probe" data is shown with the connected circles, and the autocorrelation of the rear "probe" is shown with connected crosses. The two correlation functions are very similar since they were acquired nearly simultaneously on the same set of waves. The cross-correlation of these two data series is shown by a solid curve without symbols. The positive phase lag at the maximum of the cross correlation coefficient indicates that the waves are moving in the positive x-direction.

4.4. Distribution of breaking patches

As discussed earlier: when the laser is on, the ATM produces active ranging of the distance between the aircraft and the ocean surface; when the laser is off, the ATM optics receive a reading of the surface brightness. This is equivalent to digitizing the picture of the ocean surface in real time. One application of these digital surface images is to distinguish breaking patches from the background water surface. As shown in the photograph of Figure 1b, the intensity contract between the foam produced by breaking events and the background sea water is very high. Thus a digital picture of the ocean surface can be properly thresholded to create a binary image of the ocean surface. (During the experimental period, the sky was overcast and no sun glint appeared in the images.) Statistical analysis indicates that the intensity distribution is gaussian-like. The mean and the standard deviation of the passive intensity data are calculated. The threshold is then set at a level corresponding to several standard deviations above the mean. At this stage, determination of the multiplication factor for the threshold is empirical. A limited

number of tests suggest that the magnitude of the multiplication factor is between 2 and 4. Figure 9 shows two binary images of the ocean surface brightness with thresholds set at 2.5 and 3.5 standard deviations above the mean. The two solid lines on each plot indicate the swath boundaries of the measurements. This is the same region as that of Figure 5a, but plotted in the longitude and latitude coordinates. The region is approximately 35 km offshore at 30 m water depth (the location is indicated with a circle in Figure 2). The time of the data acquisition was 09:35:16 to 09:35:36, 24 September 1997. The wind speed measured by the nearshore station at the pier end was about 9 m s^{-1}. The breaking percentage (here defined as the percentage of the water surface that appears brighter than the threshold) can be calculated from the binary images. For the two thresholds used in Figure 9, the fraction of breaking surface is found to be 0.0063 and 0.0020, respectively.

The quantitative observation of wave breaking events has been a difficult task. The data based on the measurements of whitecap coverage (e.g., Monahan 1971; Monahan and O'Muircheartaigh 1980) typically show an order of magnitude scatter (see, e.g., the data compiled in Wu 1988, Figures 1 and 2). The formula proposed by Wu (1988) for the whitecap coverage is

$$W = 1.7 \times 10^{-6} U^{3.75} \qquad (2)$$

where W is the whitecap coverage and U is the reference wind speed at 10 m elevation. For the 9 m s^{-1} wind speed, the calculated whitecap coverage is 0.0064 - in good agreement with the present processing of the passive binary image with a threshold of 2.5 times the standard deviation. The technique is promising for the study of breaking statistics in the ocean. The empirical threshold can also be compared with the corresponding measurements from video recording for further validation. This verification remains to be done.

The binary image of the breaking patches (Figure 9) provides both the statistical average and the distribution pattern of breaking waves in a given area. The image can be further combined with the ocean surface topography (Figure 5a) to yield quantitative information on the breaking distribution with respect to the wave profile. Such information offers great potential for improving our understanding of breaking waves in the ocean.

5. SUMMARY AND CONCLUSIONS

Airborne scanning lidar ranging offers a significant capability for high-resolution mapping of the wave field in the ocean. The resulting two-dimensional images of the ocean surface topography are ideal for investigating the wavenumber structure of ocean waves. The concept of applying airborne spatial wave measurements to derive source and sink functions in the energy balance equation has been tested with success using scanning radar data (Walsh et al. 1985, 1989; Hwang and Walsh 1998; Hwang et al. 1998). The resolution of the lidar data is at least one order of magnitude better than the radar data, and has been used to calibrate the radar data in the past. High resolution lidar data will extend the wavenumber coverage and increase the measurement precision.

In addition to active ranging, the scanning optical system collects passive images of surface emissivity and effectively generates instantaneous digitization of the surface brightness condition. The breaking patches show up as bright spots against the dark background of ambient ocean surface. These images can be used alone or combined with the simultaneously measured surface topography to study the wave breaking processes.

Because airborne systems provide continuous spatial coverage over a large area in a reasonably short time, there is much less variation in environmental conditions during each flight mission. The quasi-steady conditions greatly simplify the data analysis. In addition their use in investigating source and sink functions, and the spatial distribution of breaking events, the spatial measurements are effective for quantifying the shoaling wave transformation. Finally, the circular scanning measurements can be treated as paired time-lagged or space-lagged data sequences. These time/space lag measurements are suitable for the study of wave statistical properties such as the correlation and coherence functions.

APPENDIX A. DISCUSSION OF THE CIRCULAR SCANNING PATTERN

The ATM was originally designed to measure height changes in the Greenland ice cap (Krabill et al. 1995 a, b). To minimize the incidence angle dependence on the return signal, a circular scanning pattern was selected. In this scanning mode, the incident angle is maintained at a constant angle (15° in the present system). When applied to ocean wave measurements, there are a few pros and cons to this scanning pattern. These are discussed here.

To take advantage of the software developed for geophysical data analysis (for example, two-dimensional spectral analysis and image display), regridding of data into rectangular coordinates is essential. In the regridding process, duplication of data points in the new grid cells invariably occurs, representing a waste of measurement points since only one value can be kept in each cell in the final data product.

To investigate the data density issue, the locus of laser scanning is simulated for the conditions corresponding to the SandyDuck97 configuration. The airspeed V is 60 m s^{-1} and the radius of the major axis r of the locus is 100 m (corresponding to an aircraft altitude of 373 m for the 15° scanning angle). The scanning pattern repetition rate is 10 Hz and the data sample rate is 5000 Hz (10 kHz split between active and passive sensing). The coordinate (x_s, y_s) of the scanning laser spot can be expressed as

$$x_s = r\sin\theta(t) + Vt \tag{A1}$$

$$y_s = r\cos\theta(t) \tag{A2}$$

where $\theta(t)$ is the azimuthal angle of the laser spot and t is time. A small segment (200 m × 200 m) of the laser trajectories is shown in Figure A1a, and only the forward half of the trajectories is shown in Figure A1b. It is obvious that the projection of a circular scanning pattern into rectangular grids does not yield an even distribution of data density in the new grids.

Optimal grid size (Dx and Dy) can be calculated from the flight speed, aircraft altitude, scanning angle, and sample rate. The along-track grid size Dx is calculated by the distance advanced by the aircraft over one period of scan cycle. Since the aircraft velocity is 60 m s^{-1} and the period of scan cycles is 0.1 s, this distance is 6 m. The cross-track grid size is determined by the arc length of the sampling spacing. This can be approximated by $2\pi r/500$, that is, approximating the oval trajectory by a circle of radius r and dividing the circumference by the sample rate of each cycle.) With the given configurations, $Dx = 6$ m, and $Dy = 1.26$ m are chosen.

The number of data points falling into each grid can be tallied. The results are shown in Figure A2a. For each cross-track row (that is, for a given y position), the two edge cells have 11 and 12 duplicate points. The number of points per grid rapidly decreases to 1 or 2 in the majority of the central region. Altogether the 250 points in a half cycle are assigned to 160 cells in the rectangular grids, which represents a net waste of 36% of the data points. The temporal variation of sample times in the group of data within each cell is plotted in Figure A2b. The plot indicates that only the two edge cells may acquire data points from two consecutive scan lines (the time span approaches 0.1 s). For the majority of the grid cells, the data points within each cell are from the same scan line (the time span is much less than 0.1 s).

Of more concern to the analysis of ocean waves is the relative time delay across the scan line. For the mapping of fixed objects such as an ice sheet, the time delay does not pose a problem. But in the case of ocean waves that propagate with a non-negligible phase speed compared to the aircraft speed, the nonuniform cross-track time lags may introduce an error in the interpretation of the wave phase. The time lag in a cross track row with respect to the central element is plotted in Figure A2c. The data segment that is coherent to within 0.1 s is limited to the central 56% region. As the time lag allowance increases, for example in swell cases, the percentage of image region also increases. With a 0.2 s lag, the fraction is 73%, and for a 0.3 s lag, it is 89%. The maximum time lag is 0.8 s at the two edges. Therefore, if the analysis is aimed at resolving the directional properties of shorter waves, it is necessary to discard some of the data close to the swath edges.

Although the circular scanning operation introduces sampling time variability in the resampled rectangular grids, this operation mode also produces quite interesting results that are especially useful to the study of the correlation function of a wave field. As illustrated in Figure A1a, using the circular scanning mode, an area on the ocean surface covered by the front half of the laser scan will be revisited eventually by the rear half of the scan. The revisiting time is a function of the cross track coordinate (y-direction).

An easier way of visualizing the revisiting time lags is to consider the front half and the rear half of each scan cycle as bening composed of 250 pairs of probes that sample approximately the same spatial position with varying time delays. The spatial lag between each pair of laser spots that passes over a given cross-track (y) location varies from one digitization arc-length near the edges (1.3 m) of the scan locus to a spacing equal to the diameter of the minor axis of the locus at the center (200 m) of the locus (Figure A2d). The 500 data points on a scan cycle, therefore, can be decomposed into 250 measurement pairs with spatial lags shown in Figure A2d. Similarly, the scan cycles can be divided into 250 pairs from the left and right halves to form data sequences with spatial lags in the cross track orientation. The capability of obtaining such a large number of paired measurements in the ocean is quite unique. Some possible applications for such data include (1) the determination of wave propagation direction and (2) the quantitative statistical analysis of the correlation or coherence properties of a wave field.

Acknowledgment

REFERENCES

Birkemeier, W. A., and E. B. Thornton, 1994: The DUCK94 nearshore field experiment. *Proc. Coast. Dyn. '94*, 815-821.

Birkemeier, W. A., C. E. Long, and K. K. Hathaway, 1996: Delilah, DUCK94, and SandyDuck: Three nearshore field experiments. *Proc. 25th Int. Conf. Coast. Eng.*, **110**, 67-79.

Hoge, F. E., R. N. Swift, and E. B. Frederick, 1980: Water depth measurement using an airborne pulsed neon laser system. *Appl. Opt.*, **19**, 871-887.

Hwang, P. A., and E. J. Walsh, Remote sensing and coastal wave research, *Coastal Dynamics '97*, ed. E. B. Thornton, 337-345, 1998.

Hwang, P. A., E. J. Walsh, W. B. Krabill, R. N. Swift, S. S. Manizade, J. F. Scott, and M. D. Earle, 1998: Airborne remote sensing applications to coastal wave research. *J. Geophys. Res.* (in press).

Krabill, W. B., and C. F. Martin, 1987: Aircraft positioning using global positioning carrier phase data. *Navig.*, **34**, 1-21.

Krabill, W. B., R. H. Thomas, C. F. Martin, R. N. Swift, and E. B. Frederick, 1995a: Accuracy of airborne laser altimetry over the Greenland ice sheet. *Int. J. Remote Sens.*, **16**, 1211-1222.

Krabill, W. B., R. H. Thomas, K. Jezek, C. Kuivinen, and S. Manizade, 1995b: Greenland ice sheet thickness changes measured by laser altimetry. *Geophys. Res. Lett.*, **22**, 2341-2344.

Monahan, E. C., 1971: Oceanic whitecaps. *J. Phys. Oceanogr.*, **1**, 139-144.

Monahan, E. C., and I. O'Muircheartaigh, 1980: Optimal power-law description of oceanic whitecap coverage dependence on wind speed. *J. Phys. Oceanogr.*, **10**, 2094-2099.

Phillips, O. M., 1977: *The dynamics of the upper ocean.* 2nd ed., Cambridge Univ. Pub.

Schule, J. J., L. S. Simpson, and P. S. DeLeonibus, 1971: A study of wave spectra with an airborne laser. *J. Geophys. Res.*, **76**, 4160-4171.

Thornton, E. B., and R. T. Guza, 1983: Transformation of wave height distribution. *J. Geophys. Res.*, **88**, 5925-5938.

Walsh, E. J., D. W. Hancock, D. E. Hines, R. N. Swift, and J. F. Scott, 1985: Directional wave spectra

measured with the surface contour radar. *J. Phys. Oceanogr.,* **15**, 566-592.

Walsh, E. J., D. W. Hancock, D. E. Hines, R. N. Swift, and J. F. Scott, 1989: An observation of the directional wave spectrum evolution from shoreline to fully developed. *J. Phys. Oceanogr.,* **19**, 670-690.

Wu, J., 1988: Variations of whitecap coverage with wind stress and water temperature. *J. Phys. Oceanogr.,* **18**, 1448-1453.
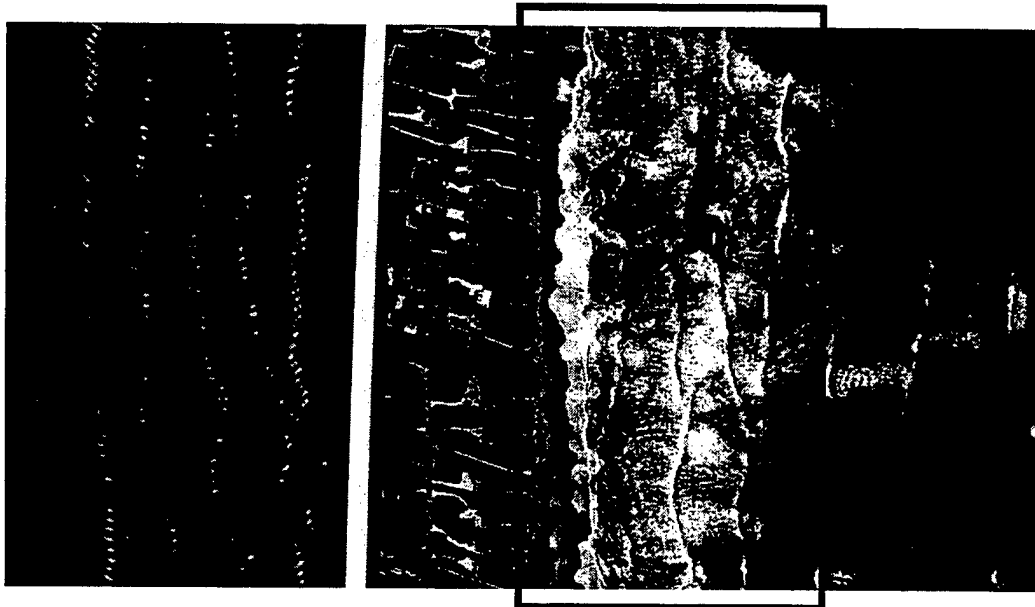
Figure 1. A comparison of the lidar measured surface topography of ocean waves (left) and the 70 mm photograph (right) taken at approximately the same time.
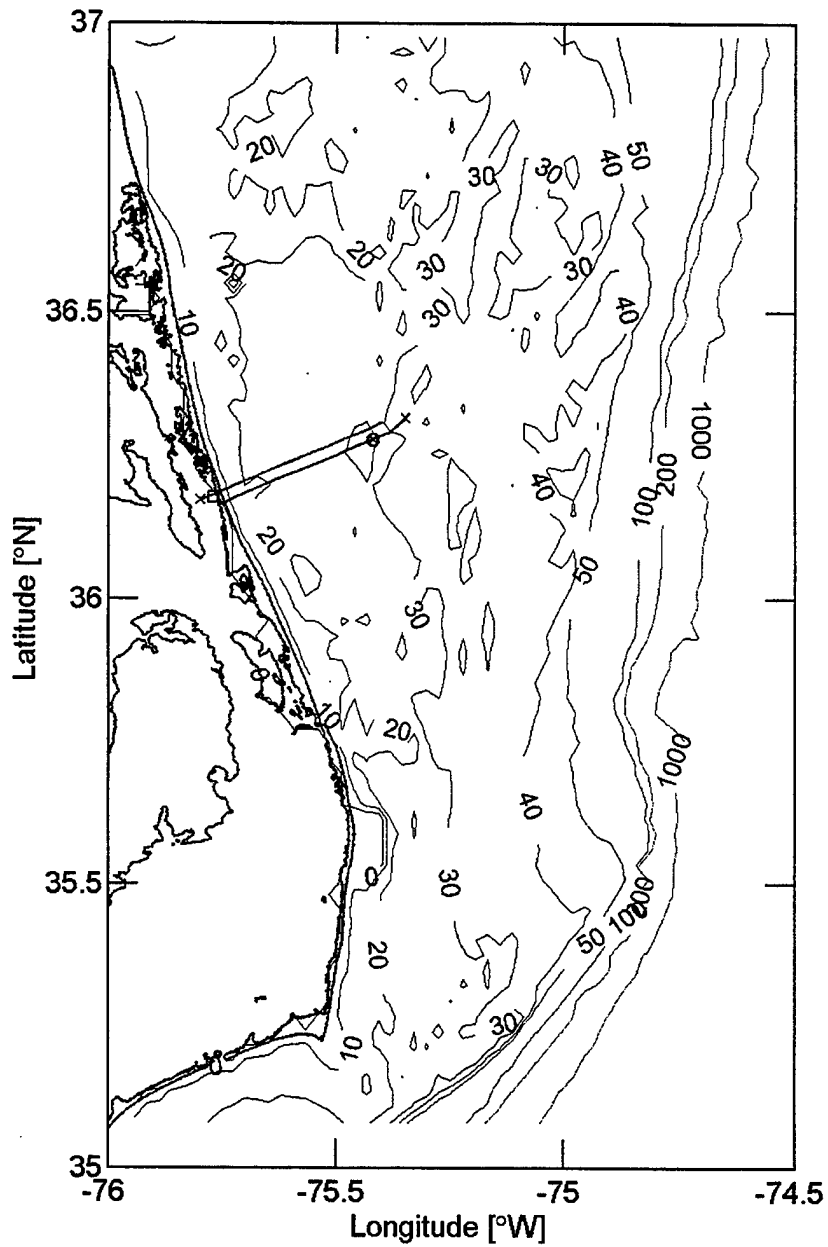
Figure 2. The flight tracks of SandyDuck97 superimposed on the coastline (dotted curve) and the bottom bathymetry of the region. The region where the images of Figures 5 and 9 were collected is indicated by a circle on the lower track. The U. S. Army Field Research Facility is shown with a square.
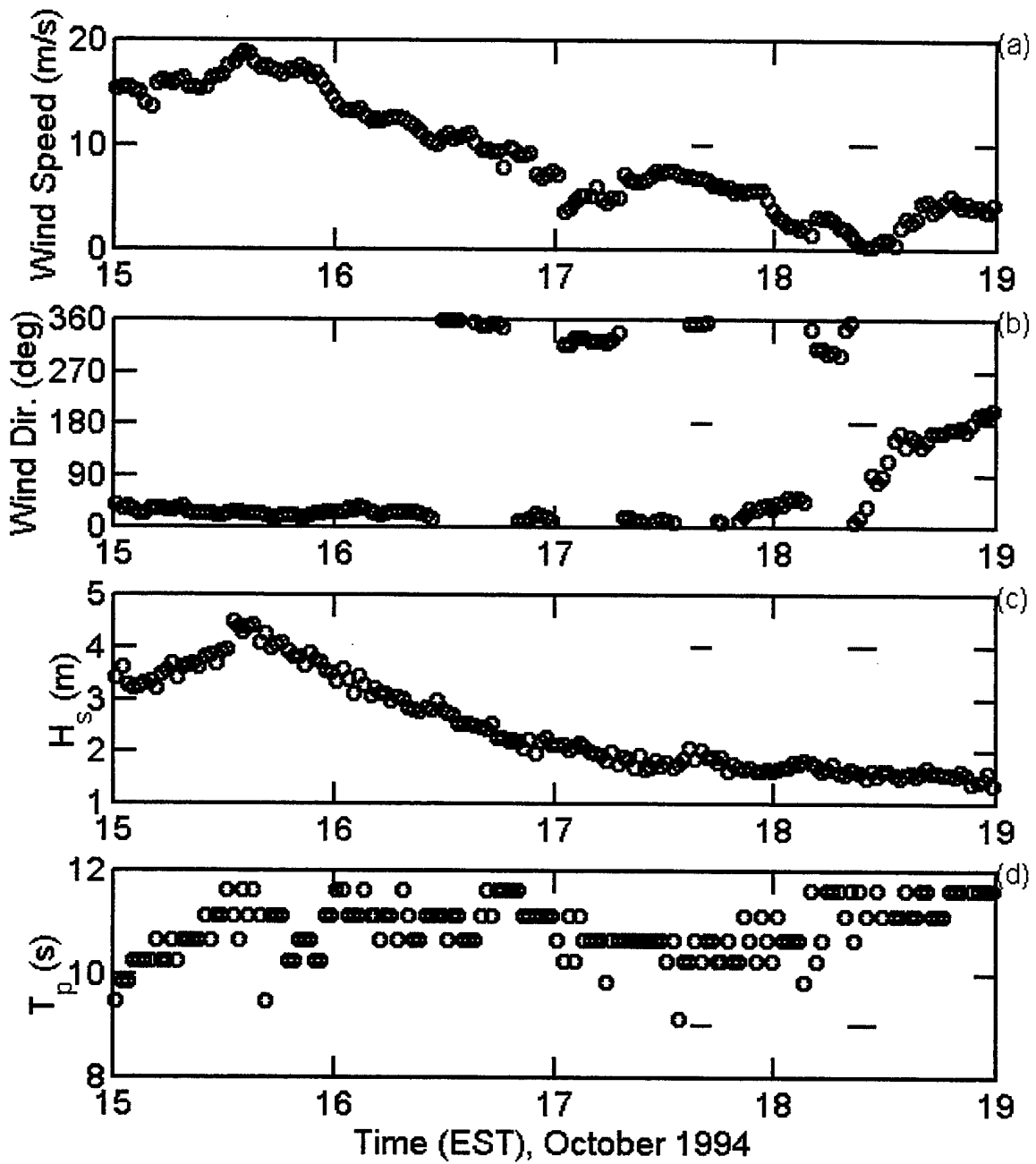
Figure 3. The experimental conditions of (a) wind speed, (b) wind direction, (c) significant wave height, and (d) peak wave period from 15-19 October 1994 of the Duck94 experiment. The short line segment on each plot represents the time of airborne wave measurements.
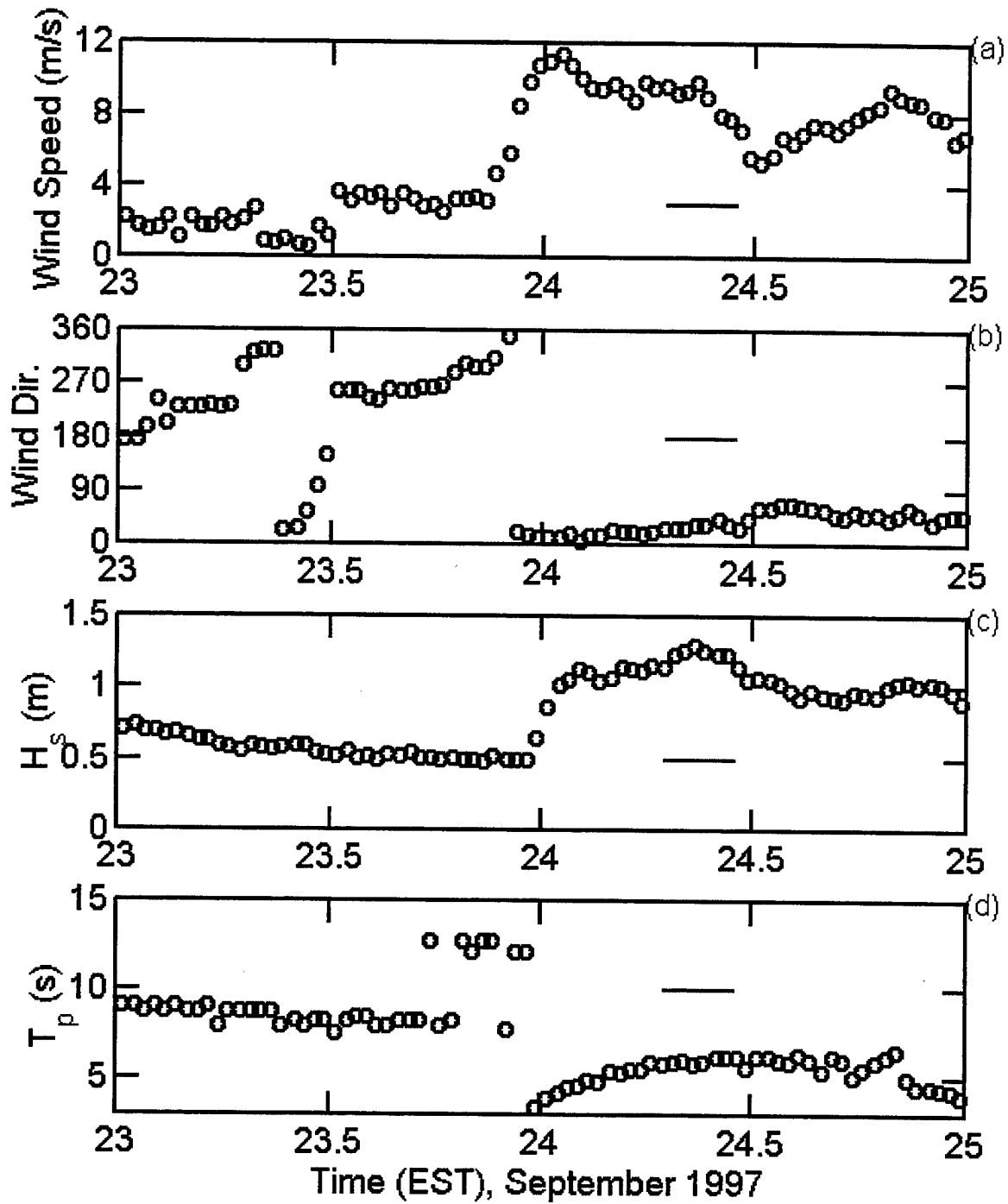
Figure 4. Same as Figure 3 but for the period 23-25 September 1997 during the SandyDuck97 experiment.

Input: 133318, 133511, 20. dx,dy: 3, 6. time,lon,lat: 133516, 36.28, 284.59, 133537, 36.28, 284.57

lidspeeg.m
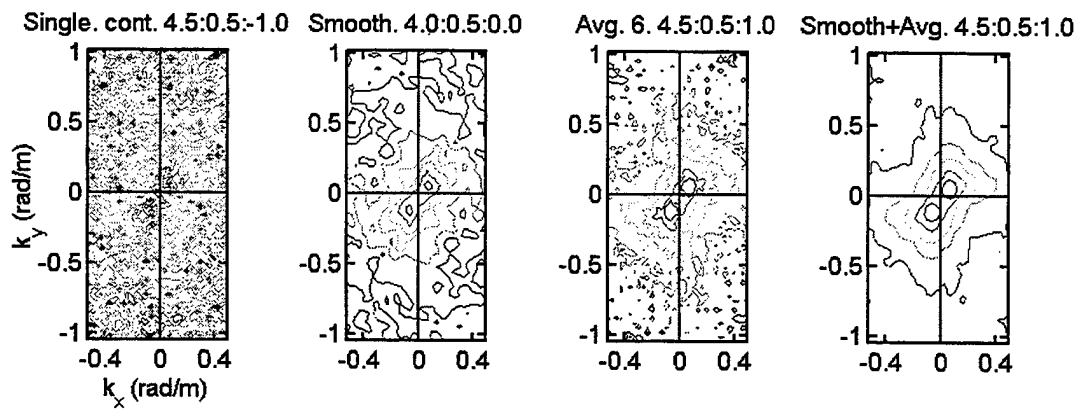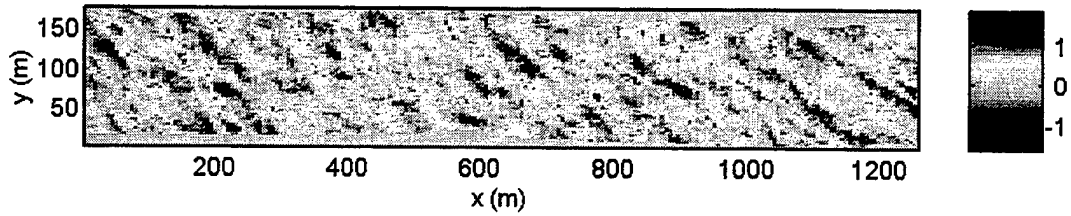
Figure 5. (a) A segment of the two-dimensional surface wave topography. The image area is approximately 180 m × 1400 m. The image is resampled from the scanning lidar data and reoriented in the rectangular coordinate system with respect to the flight tract as the *x*-direction. (b) A two-dimensional wavenumber spectrum calculated from a subsegment (180 m × 200 m) of the data shown in (a). (c) The result of 3 × 3 bin averaging to smooth the wavenumber spectrum shown in (b). (d) The ensemble average of seven spectra, each calculated from a non-overlapping segment of 180 m × 200 m wave field. (e) The 3 × 3 bin averaged spectrum of the ensemble averaged spectrum shown in (d).
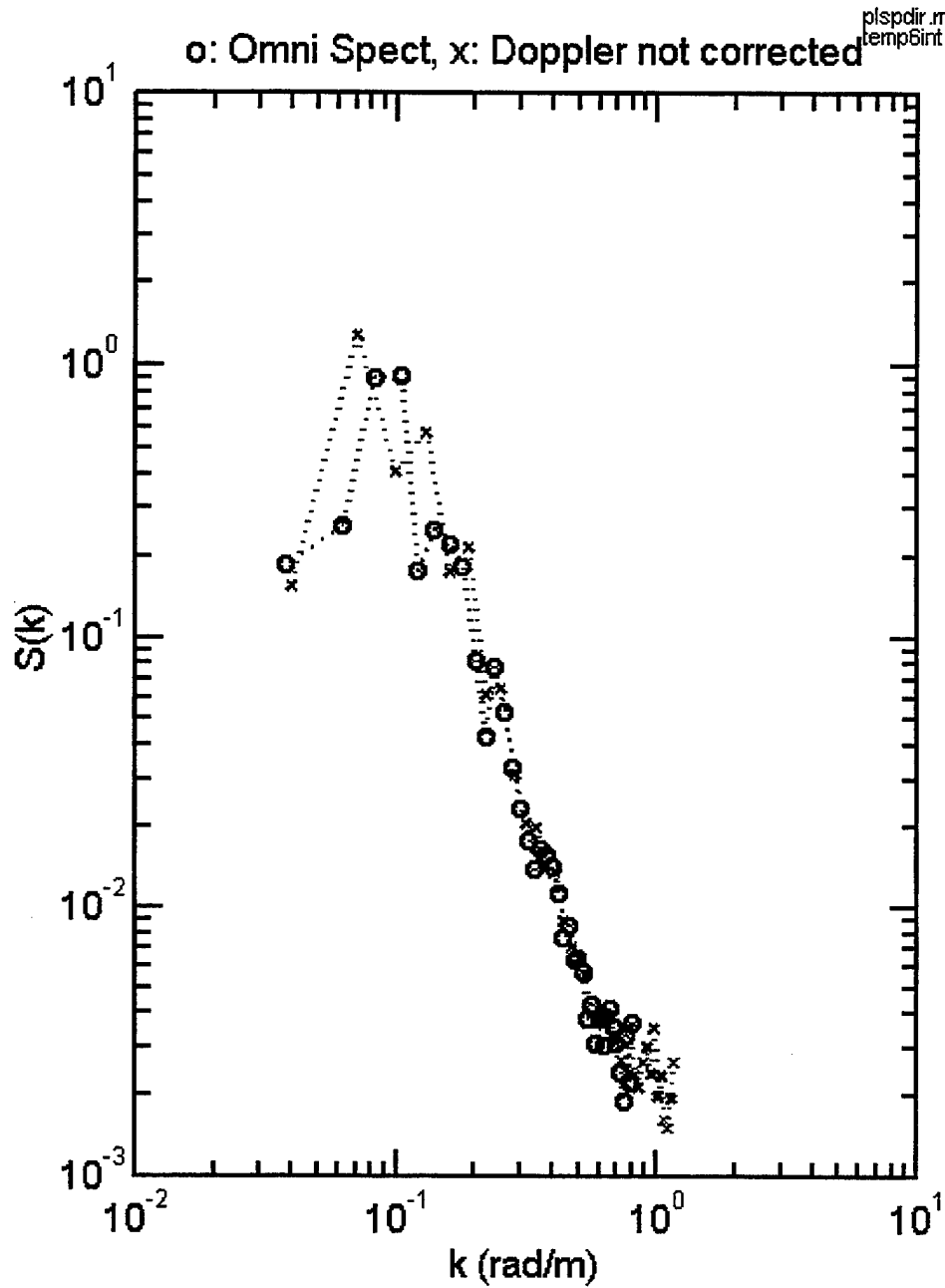
Figure 6. The omni-spectra integrated over the half-plane of the dominant spectral peak. The spectrum shown with connected circles has corrected for the Doppler shift due to the relative velocity between the aircraft and the propagating waves. The spectrum without Doppler correction is shown with connected crosses.

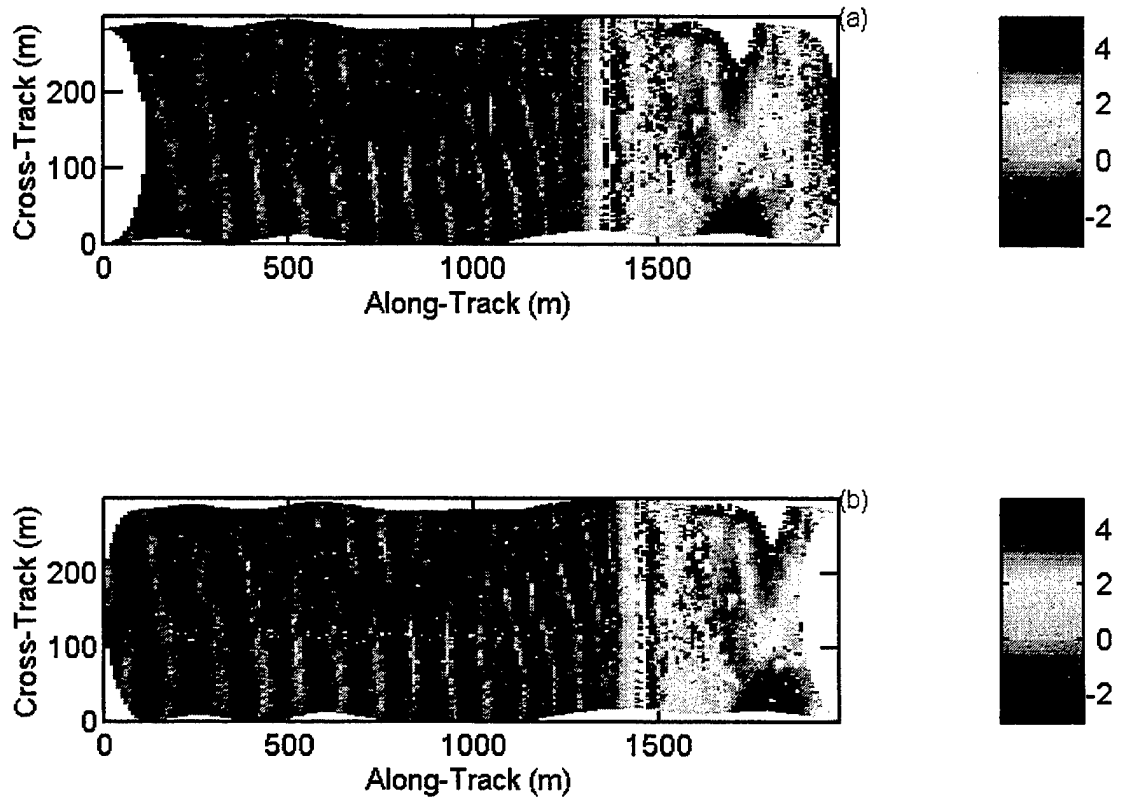Start/End time, lon, lat: 204434, 36.19, 284.26, 204454, 36.18, 284.24

Figure 7. "Time-lapsed" images of shoaling waves in the coastal region. The top image is formed from the forward scanning portion of the data and the lower image is from the aft half of the scanning data. The lapse time varies from 2 s at the center to 1/5000 s at the two edges.
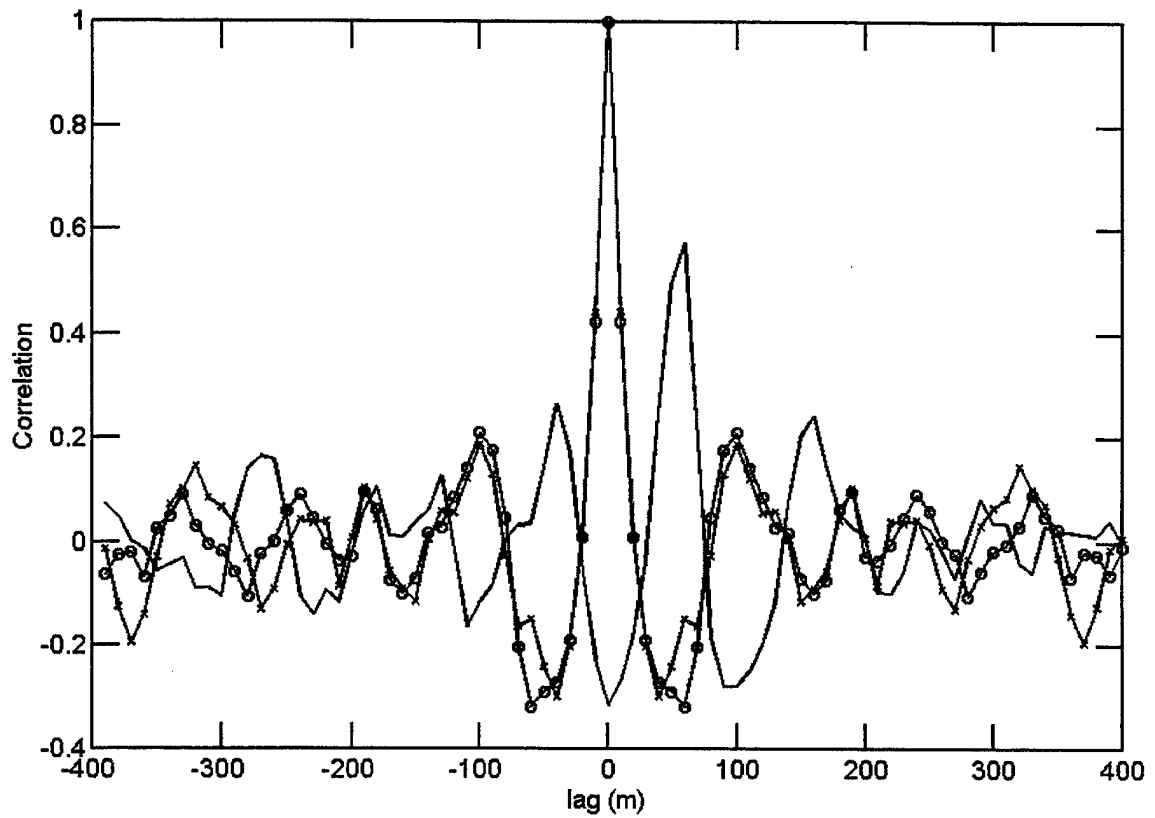
Figure 8. The autocorrelation, shown as connected circles (front element) and crosses (rear element), and the cross correlation (solid curve) of the wave profiles obtained from a pair of scanning laser "probes" constituted of one in the forward half and the other in the aft half of the scan cycle.
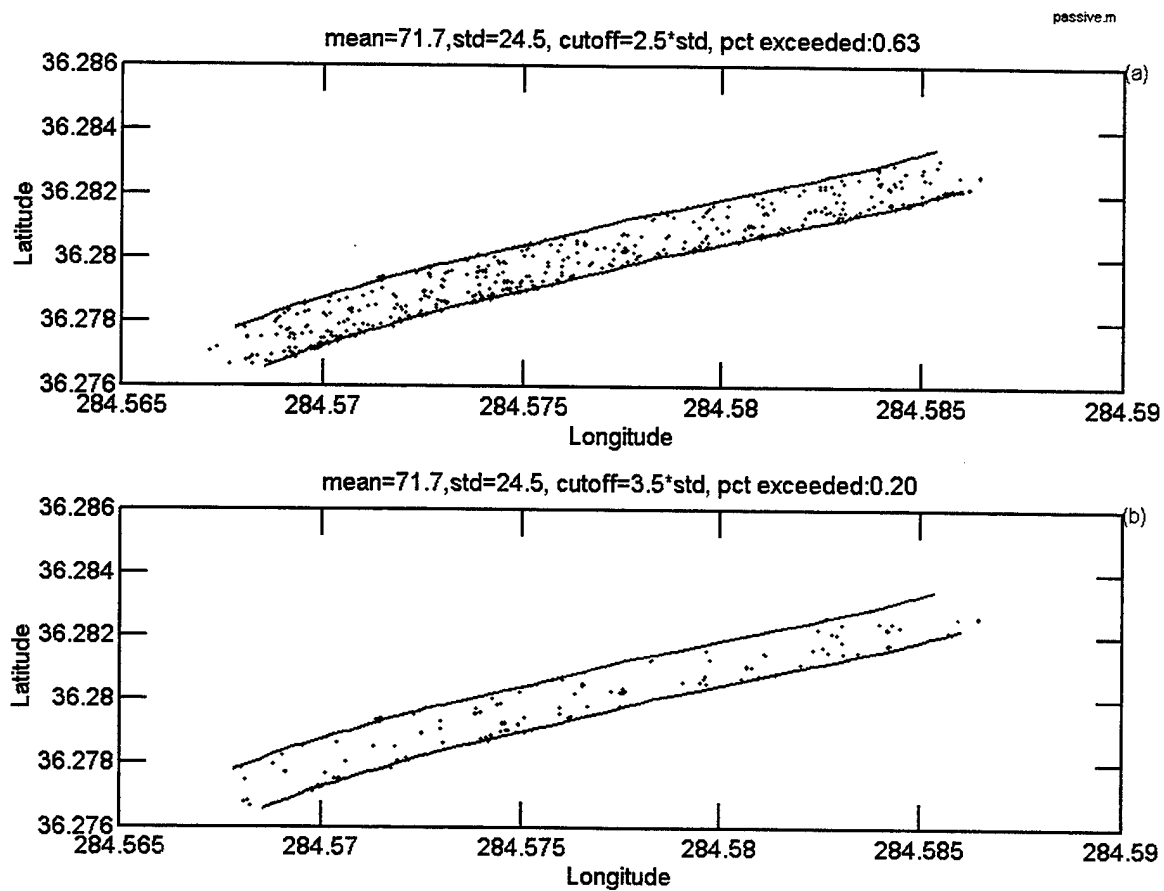
Figure 9. Binary images of the ocean surface brightness derived from the passive scanning measurements. The corresponding ocean surface topography is shown in Figure 5a. The threshold is (a) 2.5 standard deviations, and (b) 3.5 standard deviations above the mean.
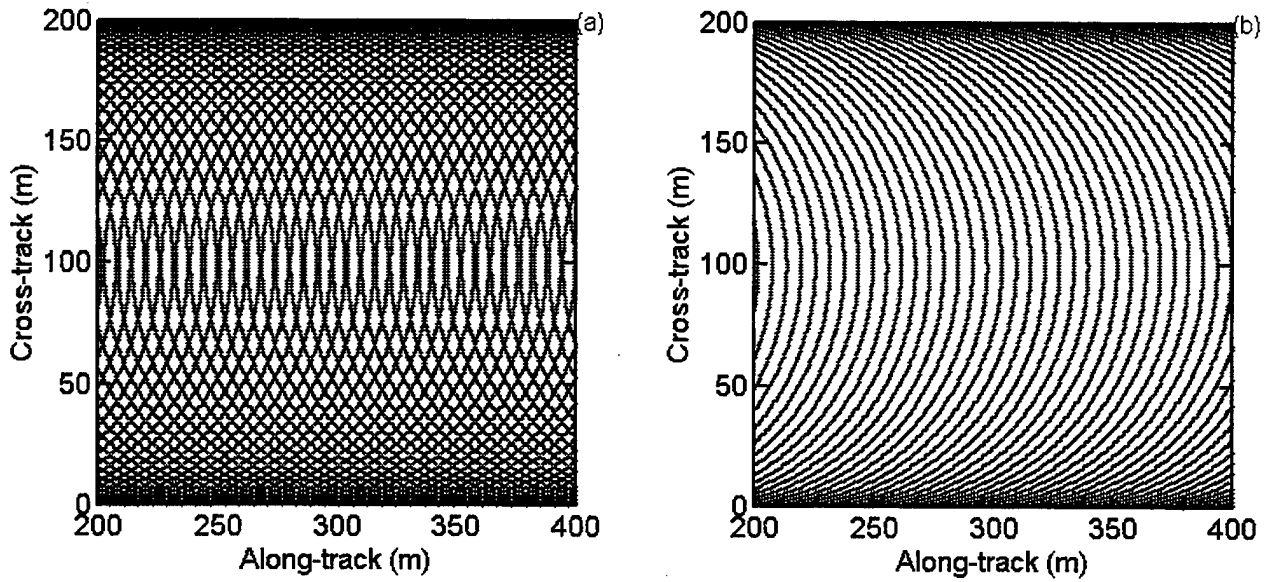
Figure A1. (a) A simulated section of the scanning lidar trajectories on the ocean surface with the flight configurations corresponds to those operated in the SandyDuck97 experiment. (b) Same as Figure A1a but only the forward halves of the scanning cycles are used.
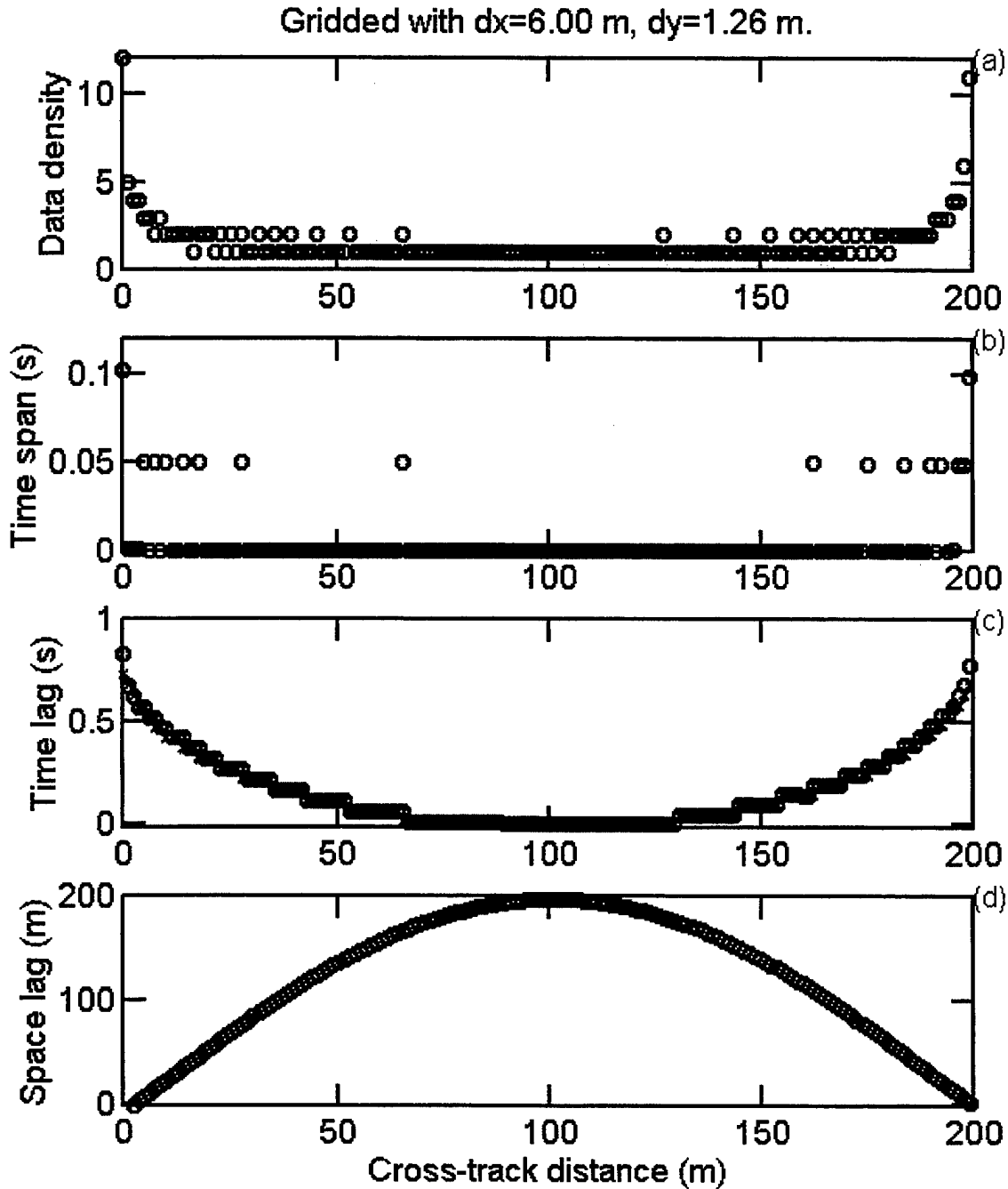
Figure A2. (a) The number of data points of the scanning measurements in each grid when resampled into rectangular coordinates. (b) The time span of the data in each grid. (c) The time lag (with respect to the central element) along a cross-track row. (d) The spatial lags of the simultaneous (within one scan cycle) laser pairs constituted of two laser beams on a scan cycle that intersects with the line y=constant.